Time-lapse imaging of seismic scattering property and velocity in the northeastern Japan

Takashi Hirose, Qing-Yu Wang, Michel Campillo, Hisashi Nakahara, Ludovic Margerin, Eric Larose, Takeshi Nishimura

Highlights

Time-lapse imaging of seismic scattering property and velocity in the northeastern Japan

Takashi Hirose, Qing-Yu Wang , Michel Campillo, Hisashi Nakahara, Ludovic Margerin, Eric Larose, Takeshi Nishimura

- Fluid migration causes changes in co-seismic scattering properties near volcanoes.
- Co-seismic velocity drops are affected by the combined effects from changes in both dynamic and static stress.
- Post-seismic relaxation of velocity is slower than scattering properties.
- Seasonal variation in the scattering properties is correlated with heavy rain and snow.

Time-lapse imaging of seismic scattering property and velocity in the northeastern Japan

Takashi Hirose[a,1,*], Qing-Yu Wang [b,c,1,**], Michel Campillo[c], Hisashi Nakahara[d], Ludovic Margerin[e], Eric Larose[c], Takeshi Nishimura[d]

[a] *National Research Institute for Earth Science and Disaster Resilience, Tsukuba, Japan*
[b] *Department of Earth, Atmospheric and Planetary Sciences, Massachusetts Institute of Technology, Cambridge, USA*
[c] *Université Grenoble Alpes, CNRS, ISTerre, Grenoble, Gières, France*
[d] *Department of Geophysics, Graduate School of Science, Tohoku University, Sendai, Japan*
[e] *Institut de Recherche en Astrophysique et Planétologie, Observatoire Midi-Pyrénées, Université Paul Sabatier, CNRS, Toulouse, France*

Abstract

Investigating spatio-temporal changes in crustal structure is a key to understanding the dynamic processes in the earth's crust associated with large earthquakes and volcanic activities. The dense seismic network in the northeast part of Japan (Tohoku region) allows us to apply the seismic interferometry to continuous recorded ambient noise data for studying crustal chages related to the 2008 M_w 6.9 Iwate-Miyagi Nairiku earthquake and the 2011 M_w 9.0 Tohoku-oki earthquake. We track for the first time the changes in both seismic scattering properties and velocities over five years, and spatially localize them based on the coda wave decorrelation and travel time sensitivity kernels calculated from the solution of the radiative transfer equation. The

[*] Corresponding author 1: Takashi Hirose
[**] Corresponding author 2: Qing-Yu Wang
Email address: takashi.hirose@bosai.go.jp (Takashi Hirose)
[1] Takashi Hirose and Qing-Yu Wang contributed equally to this work.

2008 Iwate-Miyagi Nairiku earthquake caused significant changes in both seismic scattering properties and seismic velocities in the vicinity zone of the epicenter subjected to dynamic stress perturbations. The relaxation process of elastic modulus as shown in velocity changes is slower than the recovery process of scattering properties. Changes in scattering property associated with the 2011 Tohoku-Oki earthquake around some active volcanoes in Tohoku are likely related to geofluid migrations. The decrease in seismic velocity exists mainly along the eastern coastal region and extends to the central Quaternary volcanic chains under the combined dynamic and static stress changes by the earthquake. Beyoud the significant earthquake-related changes, we observe strong seasonal changes in scattering properties due to heavy rain and snow at local scales. The waveform correlation is possibly sensitive to the fluid content and might be a useful indicator of fluid migration in the crust. This is the first time comprehensively demonstration and comparison of the spatiotemporal changes of both seismic scattering properties and velocities under the influence of the same earthquakes. We suggest that combined study of different physical parameters can reveal and help understand the crustal evolution better.

Keywords: seismic scattering property changes, seismic velocity changes, Tohoku-Oki earthquake, fluid migration, stress perturbation, seasonal variation

1. Introduction

Investigating spatio-temporal changes in crustal structure is essential to help understand the dynamic processes of large earthquakes and volcanic

activities. Seismic interferometry technique offers opportunities to track changes in crustal structure using the continuous recorded ambient seismic noise. Many previous studies reported seismic velocity changes associated with large earthquakes, and demonstrated the mechanisms responsible for the changes in seismic velocity can be dynamic stress/strain changes due to strong shaking (Brenguier et al., 2008; Schaff and Beroza, 2004; Minato et al., 2012; Brenguier et al., 2014; Wang et al., 2019), static strain changes (Wang et al., 2019), and pressurized fluids (Brenguier et al., 2014; Nimiya et al., 2017).

The seismic scattering property change, representing changes in the small-scale medium heterogeneity structure, has been estimated using the reduction in waveform correlation of seismic ambient noise CCFs. Some previous studies reported changes in seismic scattering property related to large earthquakes (Obermann et al., 2014; Hirose et al., 2020) and volcanic activities (Obermann et al., 2013; Sánchez-Pastor et al., 2019; Hirose et al., 2022). Hirose et al. (2020) reported changes in seismic scattering properties around the focal area of the 2008 Iwate-Miyagi Nairiku earthquake in the northeast part of Japan (referred to as the "Tohoku region" in this article). From the limited number of applications, the possible mechanisms of changes in the seismic scattering properties have not been systematically investigated. In contrast, many previous studies have estimated seismic velocity changes associated with large earthquakes. For example, the 2008 Iwate-Miyagi Nairiku earthquake (Takagi et al., 2012; Hobiger et al., 2012, 2014), and the 2011 Tohoku-Oki earthquake (e.g., Minato et al., 2012; Brenguier et al., 2014;

Wang et al., 2019). Moreover, seasonal changes in crustal seismic velocities were well investigated and interpreted by Wang et al. (2017). Even though these previous studies, there is no precise 2-D maps of either changes in scattering properties or velocity based on the time-lapse sensitivity kernels. Moreover, in contrast to seismic velocity changes, seasonal changes in scattering property have not yet been estimated.

This study first aims to estimate spatio-temporal changes in both seismic scattering property and velocity in the Tohoku region before and after the two big earthquakes, the 2008 Iwate-Miyagi Nairiku earthquake and the 2011 Tohoku-Oki earthquake. We simultaneously invert and and compare both temporal changes and spatial distributions of seismic scattering property and velocity. We also estimate spatio-temporal changes in seismic scattering property in a quiet period without having big event and compares them with the seasonal changes in crustal seismic velocities investigated by Wang et al. (2017). This is the first time time-lapse imaging of changes in both scattering properties and velocity.

2. Data and Methods

We use continuous seismic recordings from 121 Hi-net stations (High-Sensitivity Seismograph Network maintained by the National Research Institute for Earth Science and Disaster Resilience, NIED) shown by the blue crosses in Figure 1a. A three-component short-period seismometer is installed at the bottom of the observation well with depth larger than 100 m. The sampling frequency of the Hi-net station is 100 Hz, and the natural fre-

quency is 1 Hz. We apply seismic interferometry to seismic ambient noise data on the vertical component from 2008 to 2012. To improve the temporal stability of noise records before correlation, we apply one-bit normalization (Campillo and Paul, 2003; Larose et al., 2004), which removes some irregular events and preserves the phase of the signal during this period. Spectral whitening is also applied in the frequency band between 0.08 and 2.0 Hz to decrease the influence of persistent monochromatic noise sources (Shapiro et al., 2006; Bensen et al., 2007). We compute normalized CCFs every hour and stack them to obtain daily CCFs. The daily CCF is an approximation of the time derivative of the Green's function convolves a source term between the station pair. Figure 1b shows an exemple of a record section of seismic ambient noise CCFs stacked over five years in the 0.125–1 Hz frequency band. Wave packets of Rayleigh waves propagating at a velocity of about 3 km/s are clearly seen from the CCFs.

2.1. Measurement of changes in seismic scattering properties and seismic velocity

We measure changes in waveform coherence and travel time in the 0.125-1 Hz frequency range to follow the earthquake-related variation in both scattering properties and seismic velocities, respectively. We take the stack over the whole five years as the reference CCF and the 60-day stacked as the current CCF to measure the changes between each current CCF and the reference one.

Decoherence represents the decrease in the normalized correlation be-

tween two signals and is defined as $1 - Coherence$. We measure the Coherences from both causal and acausal parts of CCFs using a 16-s time window sliding between 64 s and 112 s after the direct Rayleigh wave arrival (3 km/s in this study) without any overlapping in the frequency domain based on the following equation:

$$Coh_{xy}(f,t) = \frac{|P_{xy}(f,t)|^2}{P_{xx}(f,t)P_{yy}(f,t)}. \quad (1)$$

$Coh_{xy}(f,t)$ is the coherence value between the signals x and y as functions of frequency f and lag time t. $P_{xx}(f,t)$ and $P_{yy}(f,t)$ are power spectral densities of x and y, respectively, and $P_{xy}(f,t)$ is the cross-spectral density of x and y. This study defines conherence as the mean value of $Coh_{xy}(f,t)$ over multiple frequencies in the 0.125-1 Hz band. Decoherence values for each lag time t ($dc(t) = 1 - Coh(t)$). Finally, we take the average over windows symmetric around zero ($(dc(t_0) + dc(-t_0))/2$). This means that three decoherence measurements were obtained from each station pair.

We check the signal-to-noise ratio (SNR) of stacked CCFs over all 16 s windows. We estimate the noise level by taking the Root-Mean-Square (RMS) amplitude from the lapse time windows +180 s to +200 s and -200 s to -180 s, respectively. The SNR is averaged around zero lag time for all windows, the same as the step of decoherence. We keep the decoherence measurements when the averaged SNRs are greater than the threshold, 2.5. The time series of decoherence is derived from the differences between measurements before and after the 2008 Iwate-Miyagi Nairiku earthquake or 2011 Tohoku-Oki earthquake, in order to focus on the coseismic change, as the

equation below:

$$dc_{12}^{obs}(t) = |dc_2^{obs}(t) - dc_1^{obs}(t)|. \quad (2)$$

$dc_1^{obs}(t)$ represents the decoherence value between the reference CCF and the 60-day stacked current CCFs before the earthquake. $dc_2^{obs}(t)$ represents the decoherence after the earthquake. In this study, we use absolute differences in decoherence values. According to Margerin et al. (2016), the decoherence is proportional to the absolute value of the difference between the intensity in a reference configuration and the intensity in a perturbed configuration where a scatterer has been added or removed. In other words, both increases and decreases in the scattering coefficient produce decoherence.

In the measurement of seismic velocity changes, we apply the doublet method (Poupinet et al., 1984; Brenguier et al., 2008; Clarke et al., 2011) in the same time windows as in the decoherence measurement, starting from 64 s to 112 s after the direct arrival of Rayleigh waves to ensure a fully scattered state. In the causal and acausal parts of the CCF, we select three-time windows of 16 s to measure the travel time shift on scattered waves. In each time window of 16 s, we use an 8 s sliding window with 60% overlap to measure the phase shift. Finally, the average value from every 16s is regarded as the travel time change corresponding to the central lapse time in the window. Using the same SNR threshold, we keep all the travel time changes in the lapse time windows when SNR is larger than 2.5.

We study the changes in both decoherence and seismic velocity related to the 2008 Iwate-Miyagi Nairiku (M_w = 6.9) and the 2011 Tohoku-Oki (M_w = 9.0) earthquakes to understand how different physical parameters evolve with time and in space. The waveform decoherence (scattering property change) is sensitive to a structural change on a scale comparable to the wavelength. The seismic velocity change is sensitive to a change on a scale longer than the wavelength. Figure 2 shows exemples of temporal changes in both coherence and seismic velocity for the station pairs N.ICEH–N.NRKH and N.ADTH–N.TSTH. Under the assumption that Rayleigh waves are predominant in seismic ambient noise CCFs, changes in coherence and seismic velocity are mainly sensitive to crustal deformation within about 8 km depth ($\lambda/3$ at 0.125 Hz).

The N.ICEH–N.NRKH station pair is located close to the focal area of the Iwate-Miyagi Nairiku earthquake and shows clear changes in both coherence and seismic velocity similar to the observations by Takagi et al. (2012); Wang et al. (2017); Hirose et al. (2020). No significant change in coherence or seismic velocity was observed at station pairs far from the epicenter. For the Tohoku-Oki earthquake-related changes, we see clear decoherence from N.ICEH–N.NRKH station pair. The amount of decoherence related to the Iwate-Miyagi Niariku earthquake is greater than that of the Tohoku-Oki earthquake, while changes in seismic velocity related to the two earthquakes are comparable. The seismic stations N.ADTH and N.TSTH are located west of the Bandai volcano in the southern part of the Tohoku region (see also Figure 1). This station pair shows clear coherence/seismic velocity drops as-

sociated with the Tohoku-Oki earthquake. Beyond those earthquake-related change, there are some seasonal coherence variation with a relatively low value in winter and summer.

2.2. Imaging of changes in seismic scattering properties and seismic velocity

Imaging of the changes in seismic scattering properties and seismic velocity measured from scattered coda waves is always challenging due to the lack of information on the sensitivity kernels of coda waves. For mapping the seismic velocity changes, people usually adopt direct interpolation to approximate the spatial velocity changes. In this paper, we calculate the analytical solution of 2-D coda sensitivity kernels based on the radiative transfer equation (Shang and Gao, 1988; Sato, 1993; Paasschens, 1997) for 2-D isotropic scattering assumption. The coda wave kernels serve as the spatial weighting function for locating both seismic scattering property changes and velocity changes (e.g., Planès et al., 2014; Larose et al., 2015).

Previous studies have reported some regional dependence of seismic attenuation structures in Japan (Hoshiba, 1993; Carcolé and Sato, 2010). Hoshiba (1993) and Carcolé and Sato (2010) also estimated S-waves' scattering mean free paths in Japan. However, the seismic scattering attenuation structures in the microseismic frequency band are still not very well known. Hirose (2019) applied passive estimation method of scattering and intrinsic absorption parameters to Hi-net data around the focal area of the Iwate-Miyagi Nairiku earthquake. The results suggest that mean free path of Rayleigh waves below 0.5 Hz are probably longer than 100 km. In this study, assuming a spatial uniformed value of scattering mean free path on the calculation

of sensitivity kernels, we keep the identical mean free path as 100 km. In scattering property change inversion, the following relationship is used:

$$\epsilon_i = G_{ij}^{\mathrm{dc}} \cdot \Delta g_j, \tag{3}$$

where $\epsilon_i = dc_i^{obs}$. i is the index of each measurement. dc_i^{obs}, observed decohrence value, was measured for each station pair and lag time. $G_{ij}^{\mathrm{dc}} = \frac{c\Delta S}{2} \cdot K_{ij}^{\mathrm{dc}}$, and j is the grid index. In this study, we divide the study area into 1891 small cells with a size of $0.10^\circ \times 0.10^\circ$ (approximately 10 km $\times$ 10 km). The cell size is much smaller than the scattering mean free path, and this is adequate for the assumption that scatterings occur only once within each cell.

For the seismic velocity change inversion, the relationship is as follows:

$$\epsilon_i = G_{ij}^{\mathrm{tt}} \cdot \left(\frac{\delta v}{v}\right)_j, \tag{4}$$

where $\epsilon_i = -\delta t_i$. i is the index of each measurement. δt_i, observed travel time change, was measured for each station pair and lag time. $G_{ij}^{\mathrm{tt}} = \Delta S \cdot K_{ij}^{\mathrm{tt}}$, and j is the grid index. The coda wave decorrealation kernel K_{ij}^{dc} and travel time sensitivity kernel K_{ij}^{tt} are defined as below (Margerin et al., 2016):

$$K_{ij}^{\mathrm{dc}}(\mathbf{r}', \mathbf{t}; \mathbf{r}, \mathbf{r_0}) = \frac{\int_{\mathbf{0}}^{\mathbf{t}} I(\mathbf{r}', \mathbf{t} - \mathbf{t}'; \mathbf{r}) I(\mathbf{r}', \mathbf{t}'; \mathbf{r_0}) \mathbf{dt}'}{I(\mathbf{r}, \mathbf{t}; \mathbf{r_0})}, \tag{5}$$

$$K_{ij}^{\mathrm{tt}}(\mathbf{r}', \mathbf{t}; \mathbf{r}, \mathbf{r_0}) = \mathbf{S^d} \int_{\mathbf{0}}^{\mathbf{t}} \int_{\mathbf{S^d}} \frac{I(\mathbf{r}', \mathbf{t} - \mathbf{t}', -\mathbf{n}'; \mathbf{r}) I(\mathbf{r}', \mathbf{t}', \mathbf{n}'; \mathbf{r_0}) \mathbf{dt}' \mathbf{dn}'}{I(\mathbf{r}, \mathbf{t}; \mathbf{r_0})}. \tag{6}$$

$\mathbf{r_0}$ and $\mathbf{r}$ indicate the locations of source and receiver, respectively. t is the lapse time. S^d represents the unit sphere in space dimension d. I stands

intensity propagator, and the intensities $I(\mathbf{r}', \mathbf{t} - \mathbf{t}'; \mathbf{r})$ and $I(\mathbf{r}', \mathbf{t} - \mathbf{t}'; \mathbf{r})$, and $I(\mathbf{r}', \mathbf{t}'; \mathbf{r_0})$ are the mean intensities, which is the angular averaged intensity. We calculated the kernels based on the 2-D radiative transfer model assuming isotropic scattering and source radiation in an infinite medium (Shang and Gao, 1988; Sato, 1993; Paasschens, 1997). The numerator of Equation 6 is a convolution between the specific intensities of two sources: the source of forward intensity and one of backward intensity. Specific intensities are calculated by Monte Carlo simulation (Margerin et al., 2016). Figure 3 shows examples of the decorrelation and travel time sensitivity kernels of coda waves for the station pair of N.ICEH–N.KMYH. Strong sensitivity mainly distribute around the two stations. The scattering kernel shows a single scattering shell edge effect at distance far away from stations, while travel time kernel gradually diminish with distance.

Using the lapse time-dependent coda wave sensitivity kernels (Equations 5 and 6), we do the 2-D inversion of seismic scattering and velocity changes measured using coda waves for multiple lapse times from 64 s to 112 s after the direct arrival of Rayleigh waves based on Equations 3 and 4. To determine the spatial distribution of the change, we adopt the least-squares solution formulated by Tarantola and Valette (1982). The misfit function is defined as:

$$F = \frac{1}{2}(\boldsymbol{\epsilon} - \mathbf{G}\mathbf{m})^{\mathrm{t}}\mathbf{C}_d^{-1}(\boldsymbol{\epsilon} - \mathbf{G}\mathbf{m}) + \frac{1}{2}(\mathbf{m} - \mathbf{m_0})^{\mathrm{t}}\mathbf{C}_m^{-1}(\mathbf{m} - \mathbf{m_0}), \qquad (7)$$

where $\mathbf{m_0}$ is a initial model vector. We use a zero vector under the assumption that Δg and $\delta v/v$ are close to zero for many small cells. $\mathbf{m}$ is the model parameter that is to be searched for explaining the observations $\boldsymbol{\epsilon}$ to within

their errors.

$$\mathbf{m} = \mathbf{m_0} + \mathbf{C_m G^t} \left(\mathbf{G C_m G^t} + \mathbf{C_d} \right)^{-1} (\boldsymbol{\epsilon} - \mathbf{G m_0}) . \tag{8}$$

The covariance operator $\mathbf{C}_\mathrm{d}$ is the diagonal covariance matrix of the data. In the scattering property change inversion, we compute the standard deviation of coherence for the period after the earthquake over the target frequency band (0.125-1 Hz), and the diagonal elements of C_d are defined by std_i^2:

$$std_i = \sqrt{\frac{1}{K} \sum_{k=1}^{K} \left(Coh_i(f_k) - \overline{Coh_i(f)} \right)^2}, \tag{9}$$

where $Coh_i(f_k)$ is coherence value at k^{th} frequency for the i^{th} measurement. K is the number of observed coherences inside the target frequency band. $\overline{Coh(f)}$ is the mean coherence over the target frequency band. Some previous studies in the laboratory used the empirical relationship, $C_d(i,i) = (0.3dc_i)^2$ (e.g., Planès et al., 2015; Xie et al., 2018). However, there is no theoretical derivation of C_d in the case of scattering property change inversion with field data as far as we know now. In the seismic velocity change inversion, C_d is defined by std_i^2 (Weaver et al., 2011), which is:

$$C_d(i,i) = std_i = \frac{\sqrt{1 - CC_i^2}}{2CC_i} \sqrt{\frac{6\sqrt{\frac{\pi}{2}}T}{\omega_c^2 \left(t_2^3 - t_1^3\right)}}. \tag{10}$$

CC_i is the correlation value of the i^{th} measurement. T is the inverse of the frequency band width. t_1 and t_2 are the starting and the ending time of measurement window over coda waves. ω_c is the angular frequency and equal to $2\pi f_c$ (f_c: central frequency, 0.56 Hz). The same $\mathbf{C}_m$ is used for both scattering property and seismic velocity changes inversions. $\mathbf{C}_m$ is the

covariance matrix for the model defined by the following equation:

$$C_m(i,j) = \left(\sigma_m \frac{\lambda_0}{\lambda}\right)^2 \exp\left(-\frac{\delta_{i,j}}{\lambda}\right). \tag{11}$$

This matrix serves as a spatial smoothing term by the correlation of neighboring grid points i and j. λ_0 is the the same scaling factor as in Obermann et al. (2019), equals to grid discretization which is typical grid spacing of 10 km in our case. λ is the spatial correlation length. σ_m is the a priori standard deviation of the model. The optimal values of the smoothing parameter σ_m and the correlation length are determined using L-curve (Hansen, 1992) by plotting the maximal velocity drop against the root-mean-square (rms) misfit defined by Equation 12, over all n measurements (see Appendix A).

$$rms = \sqrt{\frac{1}{n}(\boldsymbol{\epsilon} - \mathbf{Gm})^{\mathrm{t}}\mathbf{C}_d^{-1}(\boldsymbol{\epsilon} - \mathbf{Gm})}. \tag{12}$$

3. Spatial distribution of seismic scattering property changes in Tohoku region between 2008 and 2012

In this section, we image and interpret the spatial distributions of coseismic scattering property changes related to both the 2008 Iwate-Miyagi Nairiku ($M_w = 6.9$) and the 2011 Tohoku-Oki ($M_w = 9.0$) earthquakes.

3.1. The 2008 Iwate-Miyagi Nairiku earthquake

Figure 4a shows the spatial distributions of Δg values inverted from the decoherence within the first 60-day period after the occurrence of the 2008 Iwate-Miyagi Nairiku earthquake. We see that the scattering properties significantly change in the vicinity of the epicenter of the mainshock. The maximum Δg value in this region is roughly 9.6×10^{-4} km^{-1} ($\Delta g/g_0 = 9.6$

%), which is the largest change during the five years from 2008 to 2012. The big change disappears rapidly in the next 60-day period.

A similar result was reported by Hirose et al. (2020). They estimated the spatial distribution of seismic scattering property changes related to the 2008 Iwate-Miyagi Nairiku earthquake by applying seismic interferometry and sparse modeling to 17 Hi-net stations within 100 km epicenter of the mainshock in the 0.5-1 Hz band. They also estimated the spatial distribution of changes in seismic scattering properties using linear least-squares inversion with ℓ^2 norm regularization to validate the result of the sparse modeling. We find that the spatial distributions of the change regions estimated in this study are similar to those estimated in Hirose et al. (2020). On the other hand, the maximum Δg value by Hirose et al. (2020) was estimated to be 0.021 km^{-1} ($\Delta g/g_0 = 64$ % with the assumption $g_0 = 0.033$ km^{-1}). This value is approximately six times the estimated value in this study. As we assume that Rayleigh waves are predominant in seismic ambient noise CCFs, this difference suggests that larger changes in seismic scattering properties occurred mainly in the shallow crust. Candidates for possible causes of significant seismic scattering changes in shallow regions are strong ground motion and landslides. An accelerometer located near the epicenter (N.ICWH) recorded the largest strong motion of approximately 4,000 gal (Aoi et al., 2008). This seismic station is located inside the estimated region of large changes in seismic scattering properties. Landslides occurred particularly around the Kurikoma volcano, which was involved in the earthquake. The dimension of the largest one was estimated to be 900 $\times$ 1,300 m (Yonezawa

et al., 2010). This material weakness can be associated with changes in the seismic scattering property.

3.2. The 2011 Tohoku-Oki earthquake

Figure 4b shows the spatial distributions of Δg values for successive 60-day periods since the 2011 Tohoku-Oki earthquake. Within 60 days from the mainshock (March 12 – May 11, 2011),four regions with significant change in seismic scattering properties were estimated. The first one is located in the southern part of the Tohoku region. The maximum Δg is 3.3×10^{-4} km^{-1} ($\Delta g/g_0$ = 3.3 %) at the west of Bandai volcano. The change region in scattering properties in the northern part of the Tohoku region is widely extended. Some volcanoes (Mt. Iwate, Moriyoshi-zan, Hachimantai, Akita-Komagatake, and Akita-Yakeyama) are located in this change region. In the center part of the Tohoku region, significant scattering property changes occured in the region east to Naruko and Kurikoma volcanoes ($\Delta g \approx 1.8\times10^{-4}$ km^{-1} at maximum). A Δg that mostly equals the value in the third change region was estimated along the eastern coastline of the southern part of the Tohoku region. The Δg values in the third and fourth regions are relatively smaller than those in the previous two regions. Significant changes in the scattering property in the southern and northern Tohoku region persist until the second and third periods. Δg values of about 2.4×10^{-4} and 3.8×10^{-4} km^{-1} at maximum are estimated around the south of Mt. Iwate and south of Bandai volcano in the second and third periods. Such a lack of recovery of Δg over time is clearly different from the temporal changes in the scattering properties caused by the Iwate-Miyagi Nairiku earthquake.

In contrast, the region of change in the scattering properties in the vicinity of Naruko and Kurikoma volcanoes disappeared in the second and third periods, similar to the quick recovery of the scattering properties due to the ground motion produced by the Iwate-Miyagi Nairiku earthquake. In the case of the Tohoku-Oki earthquake, strong ground motions associated with the mainshock were recorded along the eastern coastline in the Tohoku region. Furthermore, a great aftershock (M_w = 7.1) occurred about 35 km off the coast of the Oshika Peninsula (see also Figure 1) about 1 month after the mainshock. This was an inter-slab event that can cause strong ground motions. Figure 5 shows the hypocenter locations of earthquakes with magnitudes larger than 3 in the same three time periods as in Figure 4b (https://www.data.jma.go.jp/svd/eqev/data/bulletin/hypo.html). The scattering property change in the center part of the Tohoku region can have been caused by severe damages in the shallow crust due to strong ground motion caused by the mainshock and numerous aftershocks. The temporal changes in Δg along the eastern coastline of the southern part of the Tohoku region show similar characteristics with the third change region, scattering properties in this region quickly recovered. On 11 April 2011, the M_w 6.6 Iwaki earthquake occurred at a depth of 6 km beneath this change region (see also Figure 5). Strong ground motions caused by this earthquake are possibly related to changes in scattering properties for this region.

The scattering property changes in the southern and northern Tohoku region can have been caused by fluid migration. Thery et al. (2020) conducted a laboratry experiment to compare time evolution of waveform decorrelation

and seismic velocity changes ($\delta v/v$). They installed emitter and receiver on a compact sand sample sample in a box, and gradually introduced water into the box. Time evolution of waveform decorrelation and $\delta v/v$ were measured at different water front heights. Their results indicate that fluid injection has a greater effect on waveform decorraltion than on relative velocity changes. Recently, Tonegawa et al. (2022) reported repeated waveform decorrelations of seismic ambient noise CCFs prior to or at the time of slow earthquakes in the Nankai accretionary prism, Japan. Based on the slow earthquake onset mechanism discussed in previous studies, they interpreted those decorrelation as the result of the movement of fluid in the subsurface. Hirose et al. (2022) found waveform decorrelations in seismic ambient noise CCFs at Suwanosejima volcano, Japan, that are well synchronized with tilt changes that indicate magma migration beneath the volcano. These studies suggest that waveform decoherence (decorrelation) can be a good indicator to detect fluid migration. In the case of the Tohoku-Oki earthquake, some studies reported fluid-driven seismicity after the mainshock. Regarding the significant change region in scattering properties in the southern Tohoku region, previous studies revealed that fluid-driven seismicity took place west of the Bandai volcano at depth between 6 and 12 km from just after the mainshock (e.g., Okada et al., 2014; Terakawa et al., 2013; Yoshida et al., 2016). Similar fluid-driven seismicity was also reported for the region with significant changes in scattering properties in the northern Tohoku region. Kosuga (2014) reported a seismic cluster triggered by geofluid migration around the Moriyoshi-zan volcano from about two months after the mainshock. Although deep groundwater discharge around the focal area of the M_w 6.6 Iwaki earthquake was

reported by Sato et al. (2020), changes in scattering property along the eastern coastline of the southern part of the Tohoku region did not last for a long time. Fluid migrations possibly do not mainly control scattering property changes in this region.

Significant volcanic subsidences associated with the 2011 Tohoku-Oki earthquake were detected by analyses of interferometric synthetic aperture radar (InSAR) data (Takada and Fukushima, 2013). These subsidences were of the order of 5-15 cm with horizontal dimensions of up to 15-20 km, which is explained by the deformation of magmatic and hot plutonic bodies beneath volcanoes that had subsided in response to stress changes from the earthquake.

Similarly to those previous studies, our results also imply that significant structural changes took place beneath active volcanoes in the Tohoku region associated with the Tohoku-Oki earthquake.

4. Spatial distribution of seismic velocity changes in the Tohoku region

By tracking seismic wave $\delta v/v$, we learn about changes in the physical properties of the Earth's crust caused by different tectonic and non-tectonic forcings. Under the impact of the same earthquakes, the strong $\delta v/v$ are usually spatially close to the epicenters of earthquakes and show different depth characteristics from measurement using various frequency bands (Wang et al., 2019). To make a precise spatial localization of the seismic $\delta v/v$, we first time invert both earthquakes-related seismic $\delta v/v$ with the 2-D travel time kernels of coda waves calculated from equation 6 and compare the spatio-temporal behavior of the two observations.

Figures 2c and 2d represent time-series of seismic $\delta v/v$ with 60-day temporal resolution measured in the first lapse time window, 64 s after the direct arrival of Rayleigh waves, at station pairs of N.ICEH - N.NRKH and N.ADTH - N.TSTH (Figure 2e), respectively. There is an apparent quick co-seismic travel time increase coincident with the Tohoku-oki earthquake followed by long-term logarithmic recovery procedures. We then separately invert the station-pair-based travel time perturbations into spatial seismic velocity changes using the equation 8. Unlike the changes in decoherence, the quiet period of seismic $\delta v/v$ without big event is strongly contaminated by the postseismic relaxation after big earthquakes. It is therefore challenging to observe pure seasonal effects or other effects on this basis in the noreastern Japan. Furthermore, the 60-day temporal resolution, that we use to ensure a high signal-to-noise ratio, is longer than the potential observation of

transient changes in seismic $\delta v/v$ that related to the groundwater migration after the earthquake (Wang et al., 2021). We, therefore, do not discuss the seasonal effects from seismic $\delta v/v$ in this paper.

4.1. The 2008 Iwate-Miyaki Nairiku earthquake

As described in section 3.1, we also measure seismic velocity changes related to the Iwate-Miyaki Nairiku earthquake considering a zero mean seismic velocity change before the mainshock. Figure 6a shows the inverted seismic velocity changes 0-2 months and 2-4 months after the mainshock, respectively. Based on the inflection points on the L-curve (Figure A.9), we eventually keep the roughness damping term λ as 10 km and weight term σ as 0.005. We see the most significant velocity decrease located adjacent to the epicenter of the earthquake (green star). The medium gradually recovers from the changes with time going on after the earthquake.

Compared with the map of decoherence changes, both show significant changes near the earthquake epicenter subject to the dynamic stress perturbations released by the earthquake. In contrast, the changes in scattering properties recover much faster than in seismic $\delta v/v$, which can be outlined by a logarithmic recovery (Sawazaki et al., 2009; Gassenmeier et al., 2016). The recovery process of elastic modulus in the earth's crust reveled by the changes in seismic velocity is thus slower than the recovery process of scattering properties under the impact of the same earthquake.

4.2. The 2011 Tohoku-oki earthquake

Wang et al. (2019) have shown that the spatial distribution of large $\delta v/v$ at period $1-7s$ appears to be limited to the region of strong ground shaking

due to the earthquake. By contrast, $\delta v/v$ at periods $8-30s$ sample changes in the deeper part of the crust and correlates well with the modeled static strain from viscoelastic relaxation and afterslip (Becker et al., 2018; Freed et al., 2017). The spatial distribution of seismic $\delta v/v$ obtained from linear interpolation is an approximate method that can fast map the changes. In the present research, we use the radiative transfer equation-based numerical solution (Equation 6) of the coda sensitivity kernels to first provide a more physically meaningful spatial location for velocity changes related to the 2011 Tohoku-oki earthquake.

Figure 6b represents the inverted spatial seismic velocity changes after the earthquake within the first six months in sequence. We see an apparent velocity decrease along the eastern coastal region extending to the central Quaternary volcanic chains, where volcanic areas are more susceptible under same level of stress perturbations (Brenguier et al., 2014), within the first two months after the mainshock. Then, there is a gradual recovery in seismic velocity and the biggest changes shift to the eastern coastal region with time elapsed. This shows a better spatial correlation with the map of PGV (Wang et al., 2019) compared to the direct interpolated map in 1-7s. Meanwhile, as we use later coda waves to ensure the existence of sufficient scattered waves for measuring the travel-time differences, $\delta v/v$ reflect deeper and wider spatial changes considering the depth sensitivity contributed by body waves in the later coda even it is the same frequency band as in the paper by Wang et al. (2019). We claim that the seismic $\delta v/v$ therefore result from the combined effects of both dynamic and static stress changes due to the earthquake from shallow and relatively deep parts of the crust, respectively.

5. Seismic scattering property changes in quiet periods

Estimating changes in seismic scattering properties and seismic velocities in quiet periods will be important to perform the correction required to extract solely the structural changes associated with large earthquakes and volcanic activities. Regarding seismic velocities, the effects of external environmental perturbations have been reported by many previous studies: rainfall (e.g., Sens-Schönfelder and Wegler, 2006; Meier et al., 2010; Tsai, 2011; Richter et al., 2014; Compaire et al., 2021), thermoelastic stress (e.g., Meier et al., 2010; Hillers et al., 2015), ocean loading (Wang et al., 2017), snow loading (Hotovec-Ellis et al., 2014), and atmospheric pressure (Silver et al., 2007). Evaluating such meteorological effects will be important for interpreting seismic scattering property changes as well. Seasonal crustal seismic velocity changes in Japan were already discussed in Wang et al. (2017). We estimate and study scattering property changes in quiet periods by taking the Δg values during the period after the 2008 Iwate-Miyagi Nairiku and before the 2011 Tohoku-Oki earthquakes (October 2009–March 2011).

We map the difference of Δg values averaged in winter (December–February) and summer (June–August) to check the anomaly of Δg values. In the inversion of the scattering property changes, we input the absolute values of the difference between the mean decoherence value throughout the quiet period and the coherence value every 60 days (see also Equation 2). Figure 7a shows the spatial distribution of the difference of the average Δg in winter and summer. The regions indicated by blue (red) mean that the values of Δg in winter (summer) are higher than those in summer (winter). Larger Δg values happen in winter in the north and south parts of the Tohoku region

and some inland regions. The northern part of the Tohoku region shows a significant Δg value in winter. At the south of Mt. Iwate and along the east coastline of the Tohoku region, larger Δg values happen in summer.

We computed the power spectral densities (PSDs) of time series of Δg values during the quiet period for each small cell to quantify the strength of annual and semiannual variations in Δg. Figures 7b and 7c show the spatial distribution of the strength of semiannual and annual variation of Δg, respectively. Some regions show strong semiannual and/or annual variations in Δg. In the following, we focus on "Regions 1–5" where especially strong seasonalities were estimated.

To discuss possible causes of those semiannual and annual changes in Δg values in Regions 1–5, we compare them with meteorological data. We use precipitation and snow depth recorded by the Automated Meteorological Data Acquisition System (AMeDAS) by JMA. In total, 328 AMeDAS stations are deployed in the Tohoku region. Both precipitation and snow depth data are retrieved from 94 AMeDAS stations. Figure 8 shows the cumulative precipitation (left column) and mean snow depth (right column) during each 60-day-long period in Regions 1–5. These are the averaged values from AMeDAS stations within each region. In Regions 1, 2, 4, and 5, Δg values show peaks in summer, and heavy precipitations occur in July and/or June (rainy season) in these regions. The load due to an increase in ground water can be a candidate for changes in scattering properties (Obermann et al., 2014). For Regions 1–3, heavy snowfalls occur in winter. Δg values in these regions also have clear peaks in winter, indicating that heavy snowfall can be a candidate for seismic scattering property changes in those regions. A

direct elastic loading effect due to the weight of the snowpack is one possible cause of changes in scattering properties. Snowmelt is another candidate for the cause of changes in scattering properties. Furthermore, hydrological insulation due to a snow cover can cause changes in scattering properties. Hydrological insulation impedes water infiltration and limits groundwater recharging. In contrast to Regions 1–3, Regions 4 and 5 do not show significant scattering property changes in winter. This result can be interpreted that a small amount of snowfalls in these regions will not cause scattering property changes.

In the eastern part of the Tohoku region, Wang et al. (2017) assumed that seasonal variations in seismic velocities might be related to the instantaneous elastic ocean loading effect, and there is no strong correlation with local precipitation and/or snow. As described in Section 3.2, the results of previous studies (Thery et al., 2020; Tonegawa et al., 2022; Hirose et al., 2022) imply that decorrelation is more sensitive to fluid injection than seismic velocity changes. The result of the present study and those previous ones explain why we see seasonal changes in scattering properties that are related to the observation of precipitation and snow.

Although the timings of large scattering property changes and heavy snow/precipitation are almost synchronized, the relationship between the absolute values of Δg and snow depth/precipitation amount is still unclear (see Figures S1-S5 in the Supplementary material). We introduce two examples: Figure S3b shows the spatial distributions of mean snow depth and Δg values for the 60-day period from December 16, 2009, to February 14, 2010. In this period, the mean snow depth is largest in the northern Tohoku

region (in Region 3). However, Δg values around Region 3 are relatively smaller than those around Regions 1 and 2, where smaller snow depths were observed. Furthermore, large Δg values were estimated west of Region 5, although the snow depths observed at close AMeDAS stations were small. As shown in Figure S4b, the spatial distributions of Δg and precipitation also suggest that the absolute values of Δg and precipitation amounts are not fully correlated: Although especially heavy precipitations were observed around Region 4, estimated Δg values around this region are smaller than those around Regions 1 and 5 where fewer precipitations were observed.

Such in-consistence between the absolute values of Δg and snow depth/precipitation may suggest some nonlinear effects or additional mechanisms need to be considered. In terms of snow, the physical property of the accumulated snow may affect $\delta v/v$ and Δg (e.g., Guillemot et al., 2021). The rigidity of snow is related to its density, which can vary from 40 kg/m^3 (light dry snow) to 400kg/m^3 (compacted dry snow). The snow can lead either to an increase in weight without rigidity (resulting in negative $\delta v/v$), or an increase in weight with rigidity (stability or increase of $\delta v/v$). Also, when the snow comes to the melting point, the rigidity drops to zero (wet snow) and water percolates to the ground. In that latter case, we expect a totally different behavior on surface wave propagation. Similarly, different soils and also different snows will lead to different Δg.

The lateral variation of the scattering attenuation in the Tohoku region (Carcolé and Sato, 2010) can be another candidate for such non-linear effects. Inversion with sensitivity kernels that assume a spatially uniform scattering mean free path can bias the mapping results of Δg and $\delta v/v$. Recently, van

Dinther et al. (2021) shows the impact of non-uniform scattering properties on sensitivity kernels. A fault zone or a volcano, strong scattering zone, acts as secondary sources of energy transport, and can change in the spatial distribution of sensitivity. To remedy this deficiency, we propose to follow the approaches of Hirose et al. (2020) and van Dinther et al. (2020, 2022) to estimate the local scattering mean free path using envelopes of cross-correlation functions from the seismic ambient noise. Such studies help resolve the local heterogeneity and should be further considered to build proper local sensitivity kernels and better interpret non-linear effects.

6. Discussion and Conclusion

Spatiotemporal changes in seismic scattering properties and seismic velocities in the Tohoku region, the northern-east part of Japan, were explored using seismic ambient noise CCFs and coda-wave decorrelation/travel-time sensitivity kernels. We mapped the spatial changes every 60 days from 2008 to 2012 using the 2D sensitivity kernels predicted by radiative transfer theory. The results help track and localize changes pertaining to mechanical/structural changes in the middle and upper crusts.

We observed significant changes in the scattering property and decreases in the seismic velocity around the source region of the 2008 Iwate-Miyagi Nairiku earthquake. Although the locations of the most extensive changes in the scattering properties and seismic velocities are similar, their recovery procedures are distinct. Scattering properties recover faster than the seismic wave velocity changes. The latter likely obey a logarithmic recovery law. The relaxation of the elastic modulus in the earth's crust from the seismic wave velocity changes is slower than the recovery process of scattering properties under the impact of the same earthquake. This difference is possibly attributed to the different dynamics in scattering and velocity changes; the role of fluids and stress loading, respectively.

There were also significant changes in the scattering property and decreases in seismic velocity associated with the 2011 Tohoku-Oki earthquake. The scattering properties changed considerably around some volcanoes in the northern, southern, and central parts of the Tohoku region. Change regions in scattering properties in the south and north of Tohoku include areas where fluid-driven seismicities took place after the mainshock. The scattering

properties in central Tohoku recovered in two months, similar to the case of the Iwate-Miyagi Nairiku earthquake. Temporal and spatial changes suggest that changes in the scattering properties in central Tohoku may have been affected by the strong shaking of the mainshock and numerous aftershocks. In the case of seismic velocity changes, we see an apparent velocity decrease along the eastern coastal region extending to the central Quaternary volcanic chains. We interpret it as the result of the combined effects of both dynamic and static stress changes due to the earthquake.

In quiet periods without the presence of large earthquakes, time series of changes in scattering properties show seasonal characteristics. Changes in scattering properties are more intense in winter than in summer in the south and north of the Tohoku region. Changes in scattering properties in winter might be related to snow loading, snow melting, hydrological insulation due to snow cover, and the highly variable mechanical characteristics of the snow pack. The opposite observation occurred south of Mt. Iwate and in areas along the eastern coastline of the Tohoku region, where significant changes in scattering property are subject to heavy rains in summer. Although considerable changes in the scattering properties and heavy precipitation / snow are almost synchronous, further comparative studies are needed to clarify the relationship between the absolute values of Δg and the amounts of snow depth (melt) and the amount of precipitation. Unlike changes in scattering properties, changes in seismic wave velocity are more dominated by coseismic velocity drops. We suggest that waveform decoherence is more sensitive to fluid effects than seismic velocity changes and can serve as an indicator of fluid migration in the crust. Spatiotemporal analysis of multiple physical

parameters helps us better understand and constrain changes in the crustal structure associated with seismic and volcanic activities in more detail.

CRediT authorship contribution statement

Takashi Hirose: Conceptualization, Methodology, Software, Validation, Writing original draft. **Qing-Yu Wang:** Conceptualization, Methodology, Software, Validation, Writing original draft. These two authors contributed equally to this work. **Michel Campillo:** Funding acquisition, Project administration, Supervision, Validation, Writing review & editing. **Hisashi Nakahara:** Supervision, Validation, Writing review & editing. **Ludovic Margerin:** Resources, Validation, Writing review & editing. **Eric Larose:** Supervision, Validation, Writing review & editing. **Takeshi Nishimura:** Funding acquisition, Supervision, Validation, Writing review & editing.

Declaration of competing interest

The authors declare that they have no known competing financial interests or personal relationships that could have appeared to influence the work reported in this paper.

Data availability

The Hi-net continuous seismograms were downloaded from the Data Management Center of the National Research Institute for Earth Science and Disaster Resilience (https://hinetwww11.bosai.go.jp/auth/?LANG=en). The earthquake catalog compiled by Japan Meteorological Agency (JMA) is available at https://www.data.jma.go.jp/svd/eqev/data/bulletin/hypo.html. Pre-

cipitation data at the AMeDA station maintained by the JMA are available at https://www.data.jma.go.jp/obd/stats/etrn.

Acknowledgements

We are grateful to the National Research Institute for Earth Science and Disaster Resilience for providing us with continuous seismic data. T.H. was partially supported by the International Joint Graduate Program in Earth and Environmental Science (GP-EES) of Tohoku University, and the Japan Society for the Promotion of Science (JSPS) KAKENHI Grant Number 18J10232. We also acknowledge the support from the European Research Council (ERC) under the European Union's Horizon 2020 research and innovation program (grant agreement No 742335, F-IMAGE). Further support was received from JSPS KAKENHI Grant Number JP6K05528, and also by Ministry of Education, Culture, Sports, Science and Technology (MEXT) of Japan under its Earthquake and Volcano Hazards Observation and Research Program.

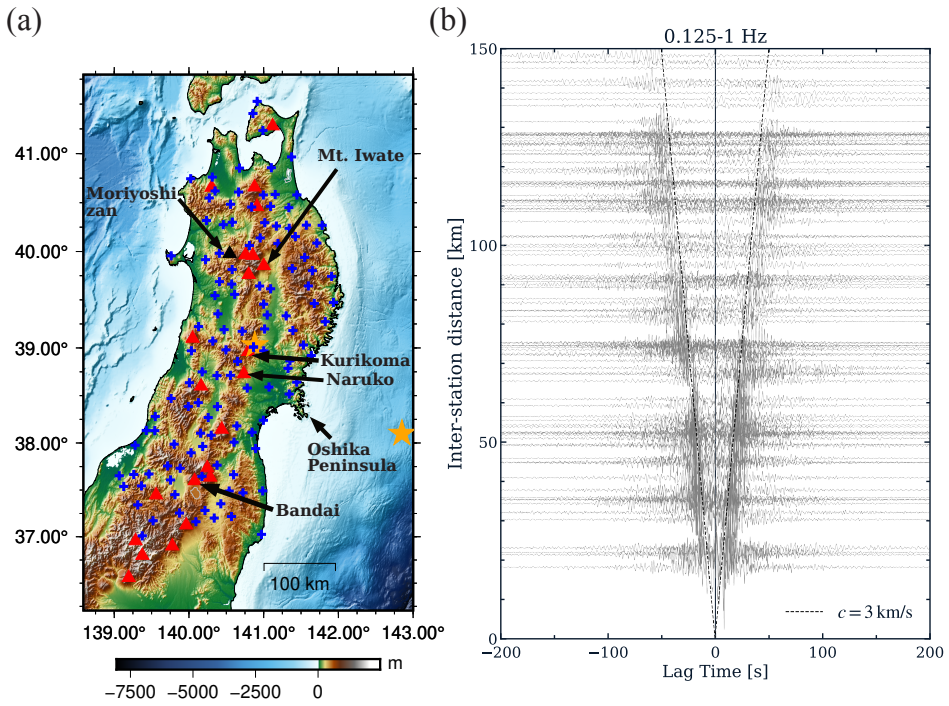

Figure 1: Deployment of seismometers and waveforms of seismic ambient noise CCFs. (a) Blue crosses represent 121 Hi-net stations installed in the north-east part of Japan (Tohoku region). The epicenter of the 2008 Iwate-Miyagi Nairiku earthquake (the 2011 Tohoku-Oki earthquake) is indicated by the yellow star at the center of the figure (at the right of the figure). Red and black triangles represent active volcanoes in the Tohoku region and Moriyoshi-zan volcano, respectively. (b) Record section of 5-year-stacked seismic ambient noise CCFs in 0.125–1 Hz band. 100 station pairs whose inter-station distances are shorter than 150 km are chosen for display. The black dashed lines represent arrival times of direct Rayleigh waves of 3 km/s.

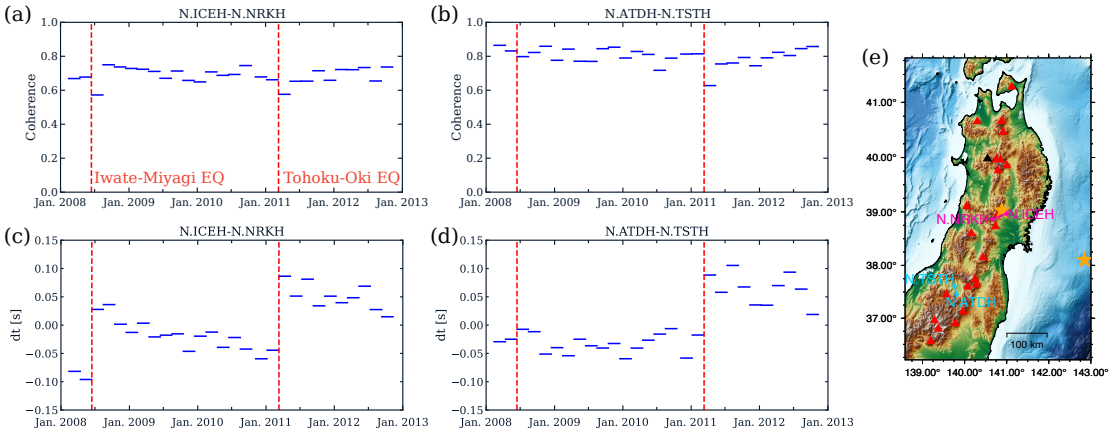

Figure 2: (a) Temporal changes of coherences per 60 days for a station pair of N.ICEH-N.NRKH. (b) Similar to (a), but for N.ADTH-N.TSTH. (c) Temporal changes of measured delay times every 60 days for N.ICEH-N.NRKH. (d) Similar to (c), but for N.ADTH-N.TSTH.. (e) Locations of N.ICEH-N.NRKH (pink line) and N.ADTH-N.TSTH (light blue line).

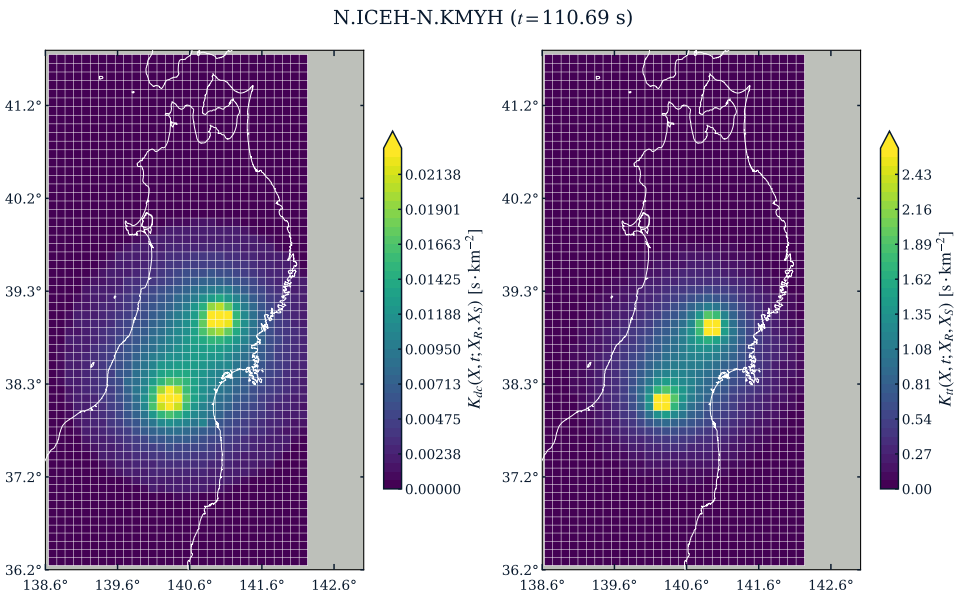

Figure 3: Examples of the decorrelation (left) and travel time (right) kernels for the station pair N.ICEH–N.KMYH at 110.69 s in lag time. These kernels were calculated assuming a scattering mean free path of 100 km.

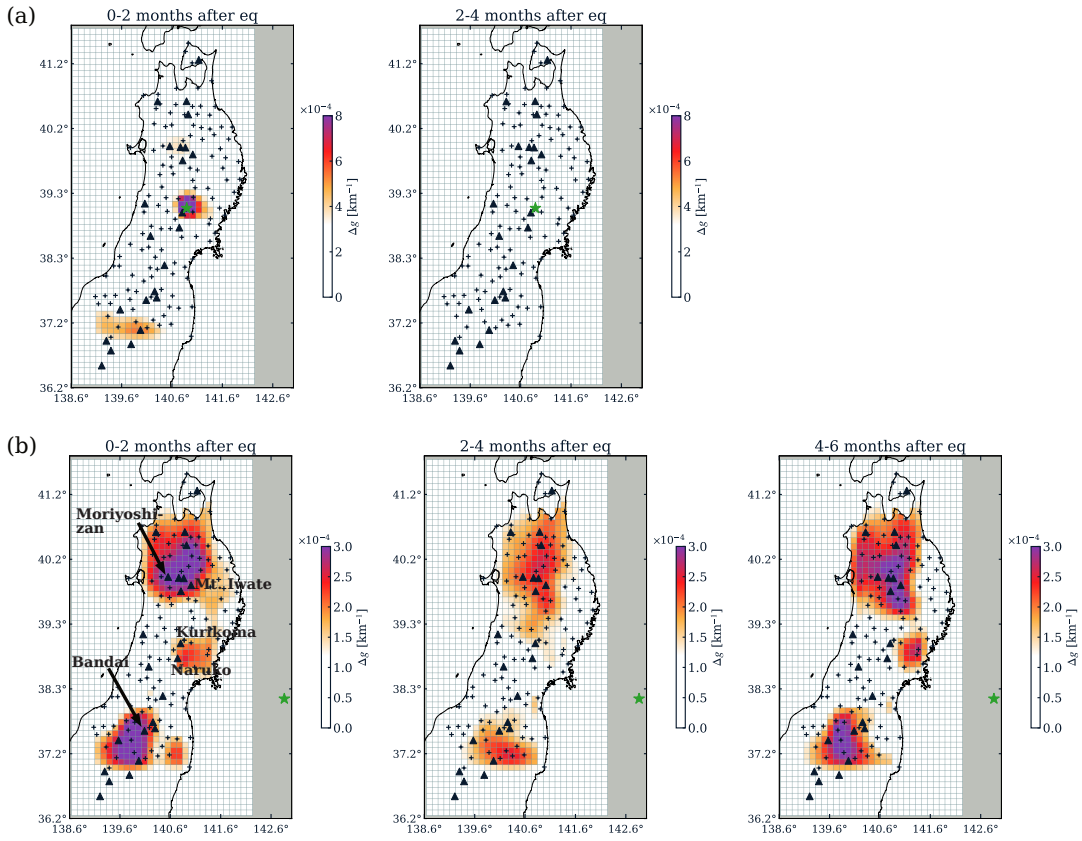

Figure 4: (a) Inverted scattering property changes after the 2008 Iwate-Miyaki Nairiku earthquake. (left) the map of Δg values 0-2 months after the earthquake. (right) the map of Δg values 2-4 months after the earthquake. The green star, black crosses, and black triangle represent the epicenter of the main shock, seismic stations, and active volcanoes, respectively. (b) Inverted scattering property changes after the 2011 Tohoku-Oki earthquake. (left) the map of Δg values 0-2 months after the earthquake, (middle) the map of Δg values 2-4 months after the earthquake, and (right) the map of Δg values 4-6 months after the earthquake, respectively. Note that the color scale is different from that of the panel (a).

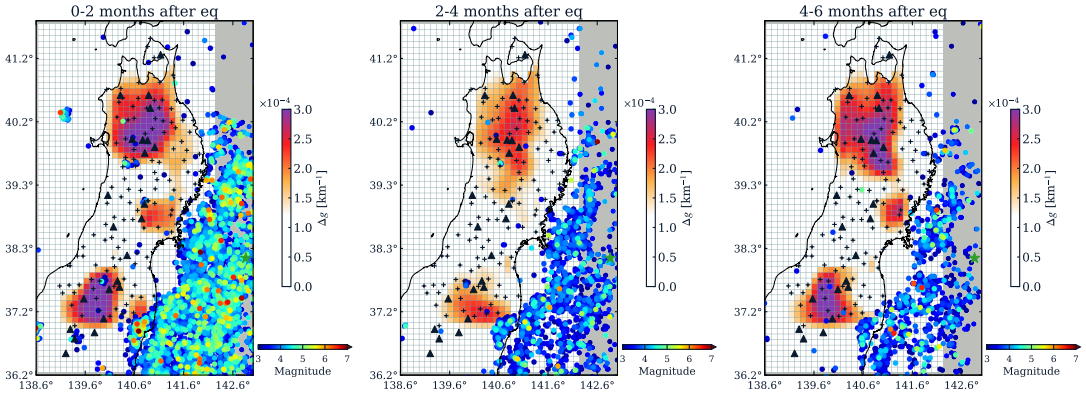

Figure 5: Hypocenters of earthquakes (M>3) in periods 0-2 months, 2-4 months, and 4-6 months after the Tohoku-Oki earthquake. Spatial distributions of scattering property changes for respective periods are also shown for comparison.

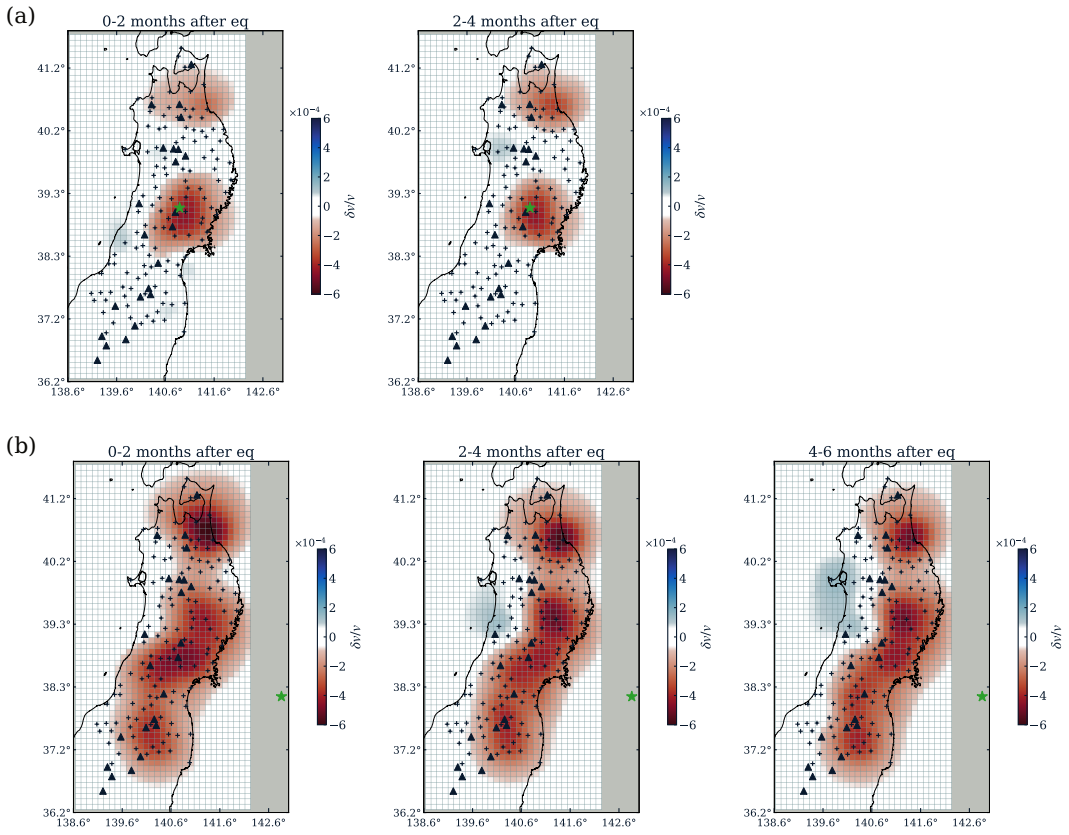

Figure 6: (a) Inverted seismic velocity changes after the 2008 Iwate-Miyaki Nairiku earthquake. (left) the map of velocity changes 0-2 months after the earthquake. (right) the map of velocity changes 2-4 months after the earthquake. (b) Inverted seismic velocity changes after the 2011 Tohoku-oki earthquake. From left to right, the panels represent the map of velocity changes 0-2 months, 2-4 months, and 4-6 months after the earthquake, respectively. Note that the color scale is different from that of panel (a).

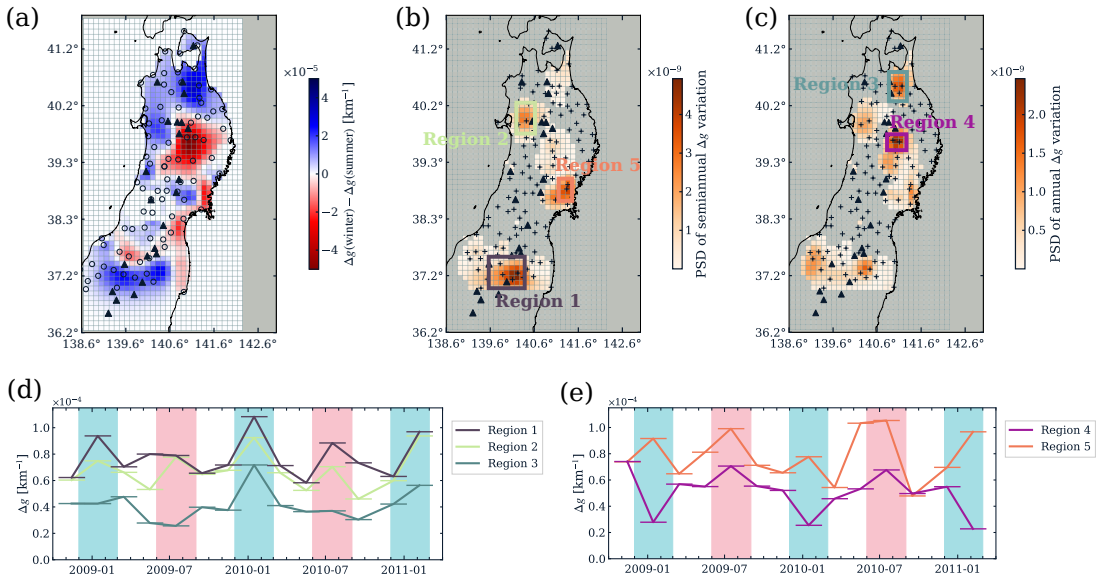

Figure 7: (a) A map of the difference in the average change in scattering coefficient (Δg) during winter and during summer. In sub-figure (a), blue/red-colored regions indicate that larger Δg values were estimated in the winter/summer season. Note that summer and winter are shown by light blue-colored and pink-colored periods in panels (d) and (e), respectively. (b) Spatial distribution of power spectral densities (PSDs) of semiannual variations in Δg. Small cells whose STD of temporal changes of Δg in the quiet periods are smaller than 1.0×10^{-5} km^{-1} are colored by gray. (c) Similar to (b), but for annual variations in Δg. (d) Temporal changes of Δg between Oct. 2008 and Mar. 2011 for three different regions (Region 1–Region 3). They are averaged for Δg values in small cells in each region. Sizes of these regions are approximately 70 km (Easting) × 60 km (Northing), 40 km × 60 km, and 40 km × 60 km, respectively. Winter (Dec.-Feb.) and summer (Jun.-Aug.) are indicated by background colors of light blue and pink. (e) Similar to (c), but for the other two different regions (Regions 4 and 5).

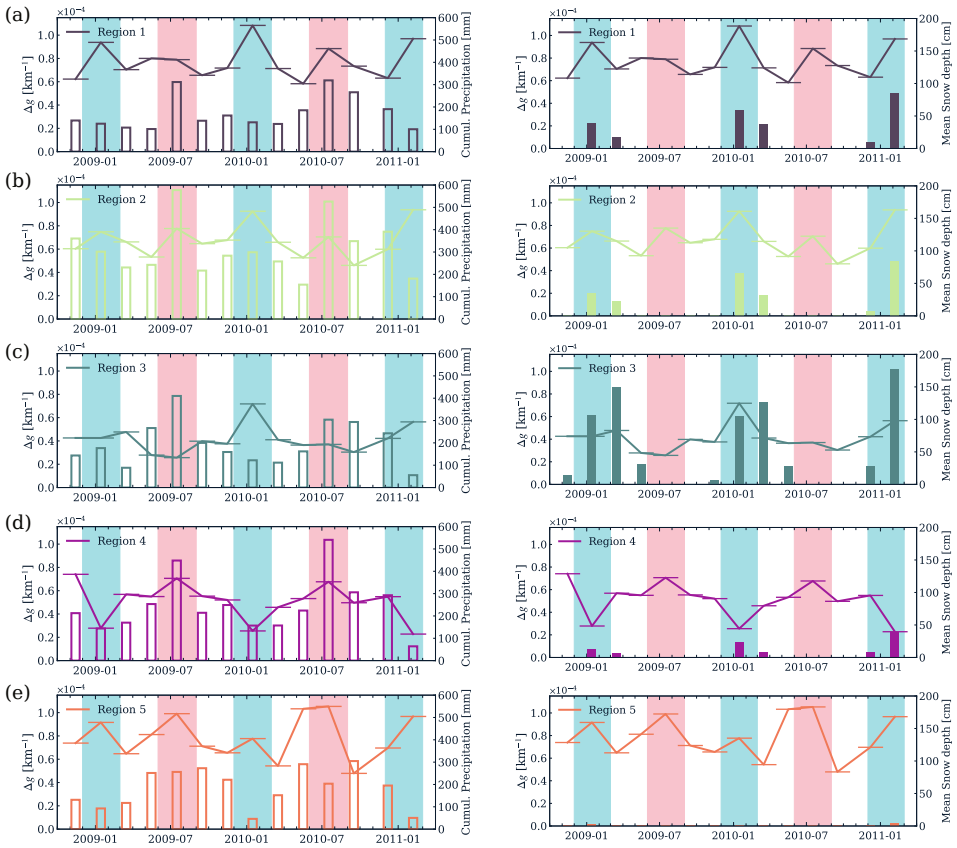

Figure 8: Comparison of temporal changes of Δg values and cumulative precipitation (left column) or mean snow depth (right column) for each 60-day period in Regions 1–5 (see Figure 7). Data of snow depths and precipitations at the Automated Meteorological Data Acquisition System (AMeDAS) station close to each region was used (https://www.data.jma.go.jp/obd/stats/etrn/).

Appendix A. Selection of optimal smoothing parameters for inversions

In the scattering property and seismic velocity inversions, we selected optimal values of smoothing parameter σ_m and the correlation length λ by using L-curve (Hansen, 1992) (see also Equation 11). Figure A.9 shows examples of L-curves in scattering property inversion and seismic velocity inversion, respectively. We tested five different λ values (λ = 10, 30, 50, 70, and 90 km), and decided to set λ = 10 km in this study.

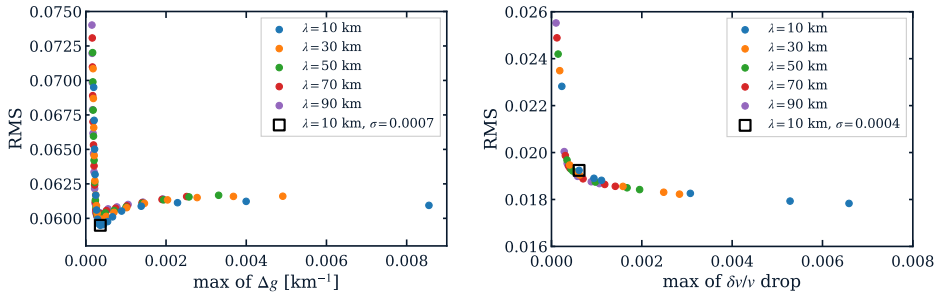

Figure A.9: L-curves. (left) Plot of rms against maximal Δg value. (right) Plot of rms against maximal drop of $\delta v/v$. The optimal λ and σ are marked by opened black squares.

References

Aoi, S., Kunugi, T., Fujiwara, H., 2008. Trampoline effect in extreme ground motion. Science 322, 727–730.

Becker, T.W., Hashima, A., Freed, A.M., Sato, H., 2018. Stress change before and after the 2011 M9 tohoku-oki earthquake. Earth Planet. Sci. Lett. 504, 174–184.

Bensen, G.D., Ritzwoller, M.H., Barmin, M.P., Levshin, A.L., Lin, F., Moschetti, M.P., Shapiro, N.M., Yang, Y., 2007. Processing seismic ambient noise data to obtain reliable broad-band surface wave dispersion measurements. Geophysical Journal International 169, 1239–1260. doi:10.1111/j.1365-246X.2007.03374.x.

Brenguier, F., Campillo, M., Takeda, T., Aoki, Y., Shapiro, N.M., Briand, X., Emoto, K., Miyake, H., 2014. Mapping pressurized volcanic fluids from induced crustal seismic velocity drops. Science .

Brenguier, F., Shapiro, N.M., Campillo, M., Ferrazzini, V., Duputel, Z., Coutant, O., Nercessian, A., 2008. Towards forecasting volcanic eruptions using seismic noise. Nat. Geosci. 1, 126–130.

Campillo, M., Paul, A., 2003. Long-Range correlations in the diffuse seismic coda. Science 299, 547–549.

Carcolé, E., Sato, H., 2010. Spatial distribution of scattering loss and intrinsic absorption of short-period S waves in the lithosphere of Japan on the basis of the Multiple Lapse Time Window Analysis of Hi-net

667 data. Geophysical Journal International 180, 268–290. doi:10.1111/j.1365-
668 246X.2009.04394.x.

669 Clarke, D., Zaccarelli, L., Shapiro, N.M., Brenguier, F., 2011. Assessment
670 of resolution and accuracy of the moving window cross spectral technique
671 for monitoring crustal temporal variations using ambient seismic noise.
672 Geophys. J. Int. 186, 867–882.

673 Compaire, N., Margerin, L., Monnereau, M., Garcia, R.F., Lange, L., Calvet,
674 M., Dahmen, N.L., Stähler, S.C., Mueller, N., Grott, M., Lognonné, P.,
675 Spohn, T., Banerdt, W.B., 2021. Seasonal variations of subsurface seismic
676 velocities monitored by the SEIS-InSight seismometer on mars. Geophys.
677 J. Int. 229, 776–799.

678 van Dinther, C., Margerin, L., Campillo, M., 2020. Laterally varying scatter-
679 ing properties in the north anatolian fault zone from ambient noise cross-
680 correlations. Geophysical Journal International doi:10.1093/gji/ggaa606.

681 van Dinther, C., Margerin, L., Campillo, M., 2021. Implications of laterally
682 varying scattering properties for subsurface monitoring with coda wave
683 sensitivity kernels: Application to volcanic and fault zone setting. J. Geo-
684 phys. Res. [Solid Earth] 126.

685 van Dinther, C., Qing-Yu, W., Margerin, L., Campillo, M., 2022. The impact
686 of laterally varying scattering properties on subsurface monitoring using
687 coda wave sensitivity kernels: Application to fault zone and volcanic areas.
688 EGU General Assembly 2022, Vienna, Austria, 23–27 May 2022, EGU22-
689 11414 doi:10.5194/egusphere-egu22-11414.

690 Freed, A.M., Hashima, A., Becker, T.W., Okaya, D.A., Sato, H., Hatanaka,
691 Y., 2017. Resolving depth-dependent subduction zone viscosity and after-
692 slip from postseismic displacements following the 2011 tohoku-oki, japan
693 earthquake. Earth Planet. Sci. Lett. 459, 279–290.

694 Gassenmeier, M., Sens-Schönfelder, C., Eulenfeld, T., Bartsch, M., Victor,
695 P., Tilmann, F., Korn, M., 2016. Field observations of seismic velocity
696 changes caused by shaking-induced damage and healing due to mesoscopic
697 nonlinearity. Geophys. J. Int. 204, 1490–1502.

698 Guillemot, A., van Herwijnen, A., Larose, E., Mayer, S., Baillet, L., 2021.
699 Effect of snowfall on changes in relative seismic velocity measured by am-
700 bient noise correlation. cryosphere 15, 5805–5817.

701 Hansen, P.C., 1992. Analysis of discrete ill-posed problems by means of the
702 l-curve. SIAM Review 34, 561–580. doi:10.1137/1034115.

703 Hillers, G., Husen, S., Obermann, A., Planès, T., Larose, E., Campillo, M.,
704 2015. Noise-based monitoring and imaging of aseismic transient deforma-
705 tion induced by the 2006 basel reservoir stimulation. GEOPHYSICS 80,
706 KS51–KS68. doi:10.1190/geo2014-0455.1.

707 Hirose, T., 2019. Development of a self-contained approach for estimating
708 space-time changes of seismic scattering properties based on seismic inter-
709 ferometry. Phd diss. Tohoku University.

710 Hirose, T., Nakahara, H., Nishimura, T., Campillo, M., 2020. Lo-
711 cating spatial changes of seismic scattering property by sparse mod-
712 eling of seismic ambient noise cross-correlation functions: Applica-

713 tion to the 2008 iwate-miyagi nairiku (mw 6.9), japan, earthquake.
714 Journal of Geophysical Research: Solid Earth 125, e2019JB019307.
715 doi:https://doi.org/10.1029/2019JB019307.

716 Hirose, T., Ueda, H., Fujita, E., 2022. Seismic scattering property changes
717 correlate with ground deformation at suwanosejima volcano, japan. J.
718 Geophys. Res. [Solid Earth] 127.

719 Hobiger, M., Wegler, U., Shiomi, K., Nakahara, H., 2012. Coseismic and
720 postseismic elastic wave velocity variations caused by the 2008 Iwate-
721 Miyagi nairiku earthquake, japan. J. Geophys. Res. 117.

722 Hobiger, M., Wegler, U., Shiomi, K., Nakahara, H., 2014. Single-station
723 cross-correlation analysis of ambient seismic noise: application to stations
724 in the surroundings of the 2008 Iwate-Miyagi nairiku earthquake. Geophys.
725 J. Int. 198, 90–109.

726 Hoshiba, M., 1993. Separation of scattering attenuation and intrinsic ab-
727 sorption in japan using the multiple lapse time window analysis of full
728 seismogram envelope. Journal of Geophysical Research: Solid Earth 98,
729 15809–15824. doi:10.1029/93JB00347.

730 Hotovec-Ellis, A., Gomberg, J., Vidale, J., Creager, K., 2014. A continuous
731 record of inter-eruption velocity change at mount st. helens from coda-
732 wave interferometry. Journal of Geophysical Research: Solid Earth 119,
733 2199–2214. doi:10.1002/2013JB010742.

734 Kosuga, M., 2014. Seismic activity near the moriyoshi-zan volcano in akita

prefecture, northeastern japan: implications for geofluid migration and a midcrustal geofluid reservoir. Earth Planets Space 66, 1–16.

Larose, E., Derode, A., Campillo, M., Fink, M., 2004. Imaging from one-bit correlations of wideband diffuse wave fields. Journal of Applied Physics 95, 8393–8399.

Larose, E., Obermann, A., Digulescu, A., Planès, T., Chaix, J.F., Mazerolle, F., Moreau, G., 2015. Locating and characterizing a crack in concrete with diffuse ultrasound: A four-point bending test. The Journal of the Acoustical Society of America 138, 232–241. doi:10.1121/1.4922330.

Margerin, L., Planès, T., Mayor, J., Calvet, M., 2016. Sensitivity kernels for coda-wave interferometry and scattering tomography: theory and numerical evaluation in two-dimensional anisotropically scattering media. Geophysical Journal International 204, 650–666. doi:10.1093/gji/ggv470.

Meier, U., Shapiro, N.M., Brenguier, F., 2010. Detecting seasonal variations in seismic velocities within los angeles basin from correlations of ambient seismic noise. Geophysical Journal International 181, 985–996. doi:https://doi.org/10.1111/j.1365-246X.2010.04550.x.

Minato, S., Tsuji, T., Ohmi, S., Matsuoka, T., 2012. Monitoring seismic velocity change caused by the 2011 tohoku-oki earthquake using ambient noise records. Geophys. Res. Lett. 39.

Nimiya, H., Ikeda, T., Tsuji, T., 2017. Spatial and temporal seismic velocity changes on kyushu island during the 2016 kumamoto earthquake. Science Advances 3, e1700813.

758 Obermann, A., Froment, B., Campillo, M., Larose, E., Planès, T., Valette,
759 B., Chen, J.H., Liu, Q.Y., 2014. Seismic noise correlations to image struc-
760 tural and mechanical changes associated with the M w 7.9 2008 wenchuan
761 earthquake. J. Geophys. Res. [Solid Earth] 119, 3155–3168.

762 Obermann, A., Planès, T., Larose, E., Campillo, M., 2013. Imaging preerup-
763 tive and coeruptive structural and mechanical changes of a volcano with
764 ambient seismic noise. J. Geophys. Res. [Solid Earth] 118, 6285–6294.

765 Obermann, A., Planes, T., Larose, É., Campillo, M., 2019. 4-D imaging of
766 subsurface changes with coda waves: numerical studies of 3-D combined
767 sensitivity kernels and applications to the Mw7.9, 2008 Wenchuan earth-
768 quake. Pure and Applied Geophysics 176, 1243–1254. doi:10.1007/s00024-
769 018-2014-7.

770 Okada, T., Matsuzawa, T., Umino, N., Yoshida, K., Hasegawa, A., Taka-
771 hashi, H., Yamada, T., Kosuga, M., Takeda, T., Kato, A., Igarashi,
772 T., Obara, K., Sakai, S., Saiga, A., Iidaka, T., Iwasaki, T., Hirata, N.,
773 Tsumura, N., Yamanaka, Y., Miyamachi, H., 2014. Hypocenter migration
774 and crustal seismic velocity distribution observed for the inland earthquake
775 swarms induced by the 2011 tohoku-oki earthquake in ne japan: Implica-
776 tions for crustal fluid distribution and crustal permeability. Geofluids 15.
777 doi:10.1111/gfl.12112.

778 Paasschens, J.C.J., 1997. Solution of the time-dependent boltzmann equa-
779 tion. Phys. Rev. E 56, 1135–1141.

780 Planès, T., Larose, E., Margerin, L., Rossetto, V., Sens-Schönfelder, C., 2014.

781 Decorrelation and phase-shift of coda waves induced by local changes: mul-
782 tiple scattering approach and numerical validation. Waves Random Com-
783 plex Media 24, 99–125.

784 Planès, T., Larose, E., Rossetto, V., Margerin, L., 2015. Imaging multiple
785 local changes in heterogeneous media with diffuse waves. J. Acoust. Soc.
786 Am. 137, 660–667.

787 Poupinet, G., Ellsworth, W.L., Frechet, J., 1984. Monitoring velocity varia-
788 tions in the crust using earthquake doublets: An application to the calav-
789 eras fault, california. J. Geophys. Res. 89, 5719–5731.

790 Richter, T., Sens-Schönfelder, C., Kind, R., Asch, G., 2014. Comprehensive
791 observation and modeling of earthquake and temperature-related seismic
792 velocity changes in northern chile with passive image interferometry. J.
793 Geophys. Res. [Solid Earth] 119, 4747–4765.

794 Sánchez-Pastor, P., Obermann, A., Schimmel, M., Weemstra, C., Verdel,
795 A., Jousset, P., 2019. Short- and long-term variations in the reykjanes
796 geothermal reservoir from seismic noise interferometry. Geophys. Res. Lett.
797 46, 5788–5798.

798 Sato, H., 1993. Energy Transportation In One- and Two-Dimensional Scatter-
799 ing Media: Analytic Solutions of the Multiple Isotropic Scattering Model.
800 Geophysical Journal International 112, 141–146. doi:10.1111/j.1365-
801 246X.1993.tb01443.x.

802 Sato, T., Kazahaya, K., Matsumoto, N., Takahashi, M., 2020. Deep ground-

water discharge after the 2011 mw 6.6 iwaki earthquake, japan. Earth Planets Space 72, 1–11.

Sawazaki, K., Sato, H., Nakahara, H., Nishimura, T., 2009. Time-lapse changes of seismic velocity in the shallow ground caused by strong ground motion shock of the 2000 western-tottori earthquake, japan, as revealed from coda deconvolution analysis. Bulletin of the Seismological Society of America 99, 352–366. doi:10.1785/0120080058.

Schaff, D.P., Beroza, G.C., 2004. Coseismic and postseismic velocity changes measured by repeating earthquakes. J. Geophys. Res. 109.

Sens-Schönfelder, C., Wegler, U., 2006. Passive image interferometry and seasonal variations of seismic velocities at merapi volcano, indonesia. Geophysical Research Letters 33. doi:https://doi.org/10.1029/2006GL027797.

Shang, T., Gao, L., 1988. Transportation theory of multiple scattering and its application to seismic coda waves of impulsive source. Scientia Sinica (series B, China) 31, 1503–1514.

Shapiro, N.M., Ritzwoller, M.H., Bensen, G.D., 2006. Source location of the 26 sec microseism from cross-correlations of ambient seismic noise. Geophysical Research Letters 33. doi:10.1029/2006GL027010.

Silver, P.G., Daley, T.M., Niu, F., Majer, E.L., 2007. Active Source Monitoring of Cross-Well Seismic Travel Time for Stress-Induced Changes. Bulletin of the Seismological Society of America 97, 281–293. doi:10.1785/0120060120.

825 Takada, Y., Fukushima, Y., 2013. Volcanic subsidence triggered by
826 the 2011 tohoku earthquake in japan. Nature Geoscience 6, 637–641.
827 doi:10.1038/ngeo1857.

828 Takagi, R., Okada, T., Nakahara, H., others, 2012. Coseismic velocity change
829 in and around the focal region of the 2008 Iwate-Miyagi nairiku earthquake.
830 Journal of .

831 Tarantola, A., Valette, B., 1982. Generalized nonlinear inverse problems
832 solved using the least squares criterion. Rev. Geophys. 20, 219.

833 Terakawa, T., Hashimoto, C., Matsu'ura, M., 2013. Changes in seis-
834 mic activity following the 2011 tohoku-oki earthquake: Effects of
835 pore fluid pressure. Earth and Planetary Science Letters 365, 17–24.
836 doi:10.1016/j.epsl.2013.01.017.

837 Thery, R., Guillemot, A., Abraham, O., Larose, E., 2020. Tracking fluids in
838 multiple scattering and highly porous materials: Toward applications in
839 non-destructive testing and seismic monitoring. Ultrasonics 102, 106019.

840 Tonegawa, T., Takemura, S., Yabe, S., Yomogida, K., 2022. Fluid migration
841 before and during slow earthquakes in the shallow nankai subduction zone.
842 J. Geophys. Res. [Solid Earth] 127.

843 Tsai, V.C., 2011. A model for seasonal changes in gps posi-
844 tions and seismic wave speeds due to thermoelastic and hydrologic
845 variations. Journal of Geophysical Research: Solid Earth 116.
846 doi:https://doi.org/10.1029/2010JB008156.

Wang, Q.Y., Brenguier, F., Campillo, M., Lecointre, A., Takeda, T., Aoki, Y., 2017. Seasonal crustal seismic velocity changes throughout japan. Journal of Geophysical Research: Solid Earth 122, 7987–8002. doi:https://doi.org/10.1002/2017JB014307.

Wang, Q.Y., Campillo, M., Brenguier, F., Lecointre, A., Takeda, T., Hashima, A., 2019. Evidence of Changes of Seismic Properties in the Entire Crust Beneath Japan After the M w 9.0, 2011 Tohoku-oki Earthquake. Journal of Geophysical Research : Solid Earth 124, 8924–8941. URL: https://hal.univ-grenoble-alpes.fr/hal-02928080, doi:10.1029/2019JB017803.

Wang, Q.Y., Campillo, M., Brenguier, F., Lecointre, A., Takeda, T., Yoshida, K., 2021. Seismic evidence of fluid migration in northeastern japan after the 2011 Tohoku-Oki earthquake. Earth Planet. Sci. Lett. 563, 116894.

Weaver, R.L., Hadziioannou, C., Larose, E., Campillo, M., 2011. On the precision of noise correlation interferometry. Geophys. J. Int. 185, 1384–1392.

Xie, F., Ren, Y., Zhou, Y., Larose, E., Baillet, L., 2018. Monitoring local changes in granite rock under biaxial test: A spatiotemporal imaging application with diffuse waves. J. Geophys. Res. [Solid Earth] 123, 2214–2227.

Yonezawa, C., Saito, G., Hori, M., Watanabe, M., 2010. Continuous monitoring of landslides area caused by iwate-miyagi nairiku earthquake in 2008 using alos images. International Archives of the Photogrammetry, Remote

870 Sensing and Spatial Information Sciences - ISPRS Archives 38, 44–47. IS-
871 PRS Technical Commission VIII Symposium on Networking the World
872 with Remote Sensing ; Conference date: 09-08-2010 Through 12-08-2010.

873 Yoshida, K., Hasegawa, A., Yoshida, T., 2016. Temporal variation of fric-
874 tional strength in an earthquake swarm in NE japan caused by fluid mi-
875 gration. J. Geophys. Res. [Solid Earth] 121, 5953–5965.